Organic Gelators as Growth Control Agents for Stable and Reproducible Hybrid Perovskite-Based Solar Cells

DOI: 10.1002/((please add manuscript number))

Article type: Full paper

Organic gelators as growth control agents for stable and reproducible hybrid perovskite-based solar cells

Sofia Masi,[a] Aurora Rizzo, [a] Rahim Munir,[b] Andrea Listorti,[a,c] Antonella Giuri, [d] Carola Esposito Corcione,[d] Neil D. Treat,[e] Giuseppe Gigli,[a,c] Aram Amassian,[b] Natalie Stingelin,[e,f]* and Silvia Colella*[a,c]*

Dr. S. Masi, Dr. A. Rizzo, Dr. A. Listorti, Prof. G. Gigli, Dr. S. Colella
Istituto di Nanotecnologia CNR-Nanotec, Polo di Nanotecnologia c/o Campus Ecotekne, Via Monteroni 73100 Lecce, Italy

Mr. Munir, Prof. A.Amassian
King Abdullah University of Science and Technology (KAUST), Physical Sciences and Engineering Division (PSE), and, KAUST Solar Center (KSC), Thuwal 23955-6900, Saudi Arabia.

Dr. A. Listorti, Prof. G. Gigli, Dr. S. Colella
Dipartimento di Matematica e Fisica "E. De Giorgi", Università del Salento, Via per Arnesano, 73100 Lecce, Italy

Mrs. A. Giuri, Dr. C. Esposito Corcione
Dipartimento di Ingegneria dell'Innovazione, Università del Salento, Via per Arnesano, 73100 Lecce, Italy

Dr. N. D.Treat, Prof. N. Stingelin

Department of Materials & Centre for Plastic Electronics, Imperial College London,

Exhibition Road, London SW7 2AZ, UK

Prof. N. Stingelin

School of Materials Science & Engineering and School of Chemical & Biomolecular

Engineering, Georgia Institute of Technology, 311 Ferst Drive, Atlanta, Georgia 30332, USA

Email: aram.amassian@kaust.edu.sa; silvia.colella@unisalento.it; natalie.stingelin@mse.gatech.edu

Keywords: halide perovskites, organic gelators, photovoltaics

Low molecular-weight organic gelators are widely used to influence the solidification of polymers, with applications ranging from packaging items, food containers to organic electronic devices, including organic photovoltaics. Here, this concept is extended to hybrid halide perovskite-based materials. In-situ time-resolved grazing incidence wide angle x-ray scattering (GIWAXS) measurements performed during spin-coating reveal that organic gelators beneficially influence the nucleation and growth of the perovskite precursor phase. This can be exploited for the fabrication of planar n-i-p heterojunction devices with $MAPbI_3$ ($MA = CH_3NH_3^+$) that display a performance that not only is enhanced by ~25% compared to solar cells where the active layer was produced without the use of a gelator but that also feature a higher stability to moisture and a reduced hysteresis. Most importantly, the presented approach is straight-forward and simple, and it provides a general method to render the film-formation of hybrid perovskites more reliable and robust, analogous to the control that is afforded by these additives in the processing of commodity 'plastics'.

1. Introduction

The recent introduction of hybrid organic-inorganic perovskites as solution-processable photoactive component for use in thin-film photovoltaic (PV) devices[1-4] has galvanized the PV community as it promises to bring to the market a low-cost, high-efficient and versatile thin-film PV technology. Thanks to the eclectic features of hybrid perovskites, various thin-film device layouts have so far been explored with the main emphasis more recently being directed on the design and processing of polycrystalline perovskite-based devices.[5-9] Thereby, much effort has been focused towards improving the surface coverage of the solution-processed perovskite active layer, *e.g.*, by increasing the size and quality of their crystalline domains.[10-12] The latter was shown to reduce the overall bulk defect density, mitigating

recombination, improving charge transport characteristics, and reducing the hysteretic behavior by suppressing ions/carriers trapping during solar cell operation.

Various strategies, such as thermal annealing,[13,14] additive inclusion,[15-18] modification of precursor concentrations and carrier solvents[19,20] and high-temperature-casting[21] have been investigated so far to control perovskite structure, grain size, degree of crystallinity and stability to moisture – however with varying success.[21,22] Here, we introduce the use of commercially available, low molecular-weight organic gelators (LMOGs), namely 1,3:2,4-di-O-methylbenzylidene-D-sorbitol (MDBS) and 1,3:2,4-di-O-dimethylbenzylidene-D-sorbitol (DMDBS) (Figure 1), to gain control over the solidification of $MAPbI_3$ and to establish a means for controlling its structure, properties and stability in the context of perovskite solar cells.

LMGOs are commonly used additives in the commodity plastics area because they promote – already at minute quantities – gelation of polymer solutions or melts upon cooling while they have no effect on these systems at elevated temperatures.[23] LMOGs are, thus, used in a number of industrial applications,[23] thanks to their easily tunable molecular structures that makes them compatible with a wide range of plastics. More recently, they proved to be useful in controlling the solidification of organic PV blends and a range of organic semiconductors, small-molecular and polymeric, where they acted as nucleating agent.[24]

Amongst the plethora of LMOGs that are commercially available, 1,3:2,4-di-O-benzylidene-D-sorbitol (DBS) and its derivatives are some of the most versatile gelators because they feature hydrophobic phenyl rings in combination with polar hydroxyl groups making them compatible with a wide range of materials of varying polarity. The assembly of LMOGs is dynamic and reversible, and it involves the formation of a hydrogen bond network [25] caused by *(i)* the presence of these terminal hydroxyl groups and *(ii)* the specific molecular geometry of DBS derivatives (Figure 1). This assembly promotes the aggregation of nanoscale fibers and the gelation of the solvent that leads to crystal nucleation in many plastics.

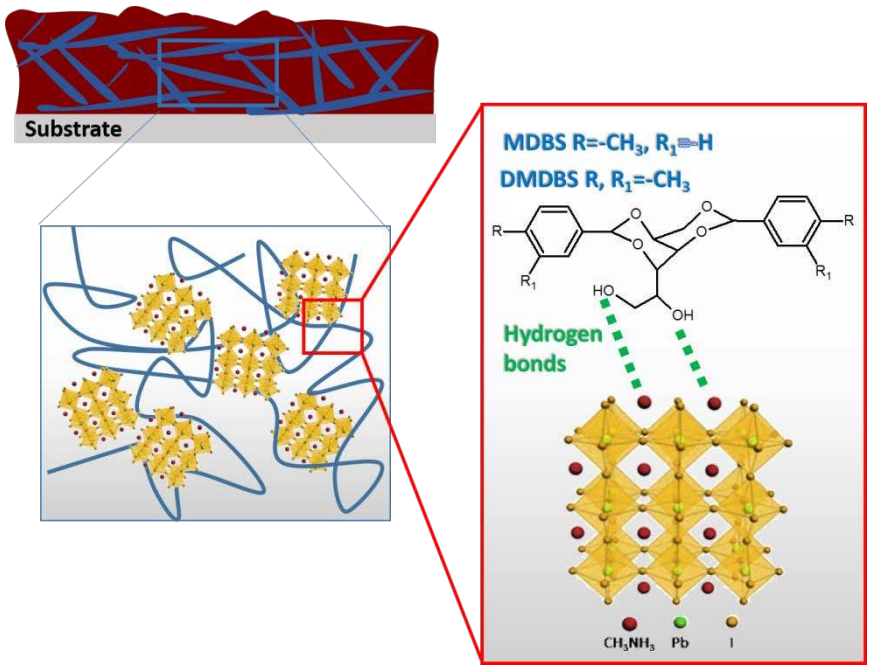

Figure 1. Schematic illustration of the supramolecular assemblies that seem to form within the perovskite precursor solutions between the inorganic component and the organic gelator molecules such as MDBS and DMDBS used in this study.

The question remains, however, whether these useful additives also can be exploited for controlling the solidification of other materials than plastics, including inorganic/organic hybrid materials such as hybrid perovskites.

Here we demonstrate the reproducible fabrication of highly efficient and stable $MAPbI_3$-based solar cells by introducing a very small quantity of organic gelator as additive to the hybrid perovskite precursor solution. We show that analogous to the use of this additive in combination with the bulk commodity polymer isotactic polypropylene (*i*-PP) or a range of organic semiconductors,[24] a small quantity of specific LMOGs is sufficient to control the sol-gel precursor as well as nucleation and solid-state structure formation of the active hybrid perovskite layer, providing a tool to control the resulting solid-state microstructure of the perovskite phase. Using a combination of rheometry data and in-situ x-ray diffraction measurements performed during spin-coating of the active layer, we show that one LMOG

studied here, *i.e.* MDBS, forms within the precursor solutions a three-dimensional network that is stabilized thanks to very specific and balanced supramolecular interactions of this additive with the precursor solvate phase. This network impacts the polycrystalline film formation of the hybrid perovskite, leading to a very compact array of crystalline domains. Noticeably, addition of MDBS seems to lead to the formation of a thermodynamically more stable perovskite thin-film structure, as our thermal analysis data indicates. Device performance is thereby not compromised: planar *n-i-p* heterojunction devices including thin and semitransparent $MAPbI_3$ layers, thus suitable for building integration purposes, have been fabricated with and without MDBS, displaying increased device performance from 11.5% (reference device without additive) to 14.5% (with MDBS). We highlight that this is the highest efficiency reported so far for solar cells comprising a relatively thin (i.e. 160 nm) perovskite layer,[26] making the use of sorbitol derivatives very promising for semitransparent solar cells. In addition, a notably decreased device-to-device performance variation and a reduced hysteresis are observed for the devices comprising the LMOG. Equally important, the introduction of a small amount of LMOG lowers the crystallization temperature of the perovskite system to below 100°C, which assists in controlling the solidification processes. Also, the stability to moisture seems to increase. These features combined with the relatively high photovoltaic efficiency make the use of LMOGs a simple and effective method foreseeing relevant industrial applications of perovskite solar cells.

2. Results and discussion

Gelation behavior of perovskite solutions containing LMOGs

Methyl-substituted derivatives of DBS are frequently used to gel polar aprotic solvents. Hence, we selected two common DBS derivatives – *i.e*. MDBS and DMDBS – as they can be dissolved into solvent systems such as 2:1 γ-butyrolactone-dimethylsulfoxide (γBL-DMSO), often used to deposit the $MAPbI_3$ precursor. Since MDBS and DMDBS are slightly apolar,

their solubility in γBL-DMSO especially at lower temperatures is somewhat limited. This ensures that the solvent mixture can be gelled.[27] We first tested the gelling ability of either DBS derivative by adding 0.1wt%, 0.5wt% or 1wt% of these LMOGs to γBL-DMSO, followed by heating these mixtures to 125 °C while stirring until clear solutions were obtained. Cooling these solutions to room temperature, we find that MDBS forms a relatively weak gel, while DMDBS forms a mechanically more stable gel (Figure S1a, Supporting Information). When the LMOGs were added to perovskite precursor (PbI_2 + MAI) solutions, using again different LMOG concentrations (0.1wt%, 0.5wt% or 1wt%), beneficially, no immediate gel formation was found to occur after cooling. Also, the cooled solutions appeared to be of lower viscosities compared to systems where no perovskite precursor had been added. We attribute this behavior to the fact that the gelation behavior of LMOGs in a complex environment of solvated salts often is different when compared to a scenario where they are used in a solvent system without salts.[27] This could be a beneficial finding when formulating 'inks' that are compatible with solution-based coating and manufacturing methodologies as undesirable, early-stage gelation can be prevented.[23]

To quantify the above observations and to obtain further information on the potential network formation of the LMOGs and how this changes the interplay between the solvent molecules and the $MAPbI_3$ precursors,[28,29] we measured the variation of the complex dynamic viscosity (η^*) of $MAPbI_3$, $MAPbI_3$-MDBS and $MAPbI_3$-DMDBS solutions with frequency (Figure 2a), as well as their frequency-dependent storage (G') and loss (G'') moduli (Figure 2b-d). A detailed discussion about these measurements is provided in the experimental section, while the shear viscosity for the three systems is supplied in the Supporting Information (Figure S2). We observe that the addition of DBS derivatives to the $MAPbI_3$ solutions significantly increases their complex viscosity in the frequency range analyzed, supporting our visual observations that the LMOGs have a notable gelating ability on the perovskite solutions. We

attribute this fluid dynamical behavior to the well-known tendency of sorbitol derivatives to form a nanofibrillar network in a range of solvents,[23] as schematically depicted in Figure 1a. More insights can be gained when comparing the storage and loss moduli of the pristine perovskite precursor solution with solutions containing MDBS or DMDBS (Figure 2b-d). For the pristine solution, the loss modulus G″ exceeds the storage modulus G′ over most of the frequency range that we measured. Moreover, both moduli strongly vary with frequency. This response indicates that the $MAPbI_3$ solution behaves as a low viscosity liquid,[30] which is in agreement with our visual observations that these solutions were free-flowing. In strong contrast, the MDBS and DMDBS solutions show gel-like responses: G′ is larger than G″ over the entire range of frequencies investigated here, indicating a dominant elastic behavior.

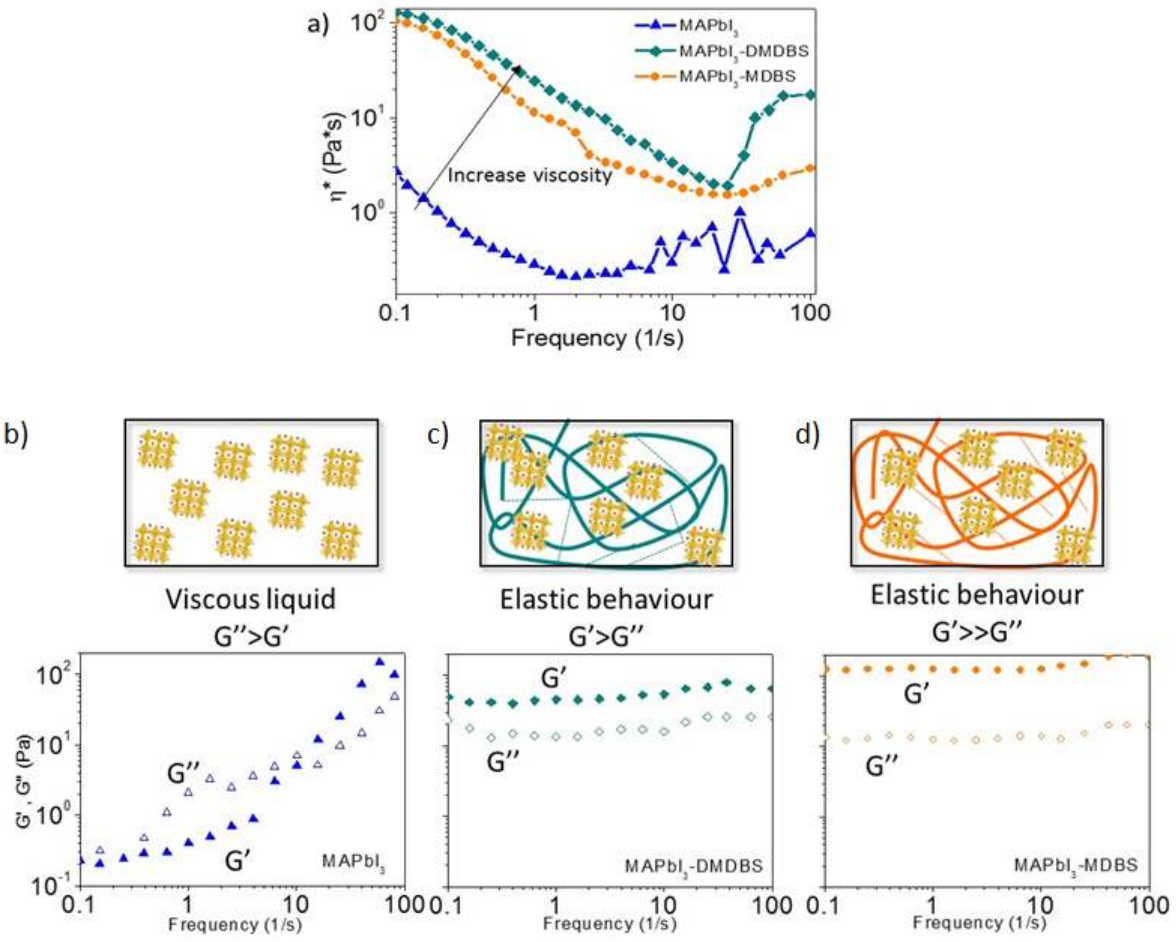

Figure 2. (a) Complex viscosity of perovskite precursor solutions to which 0.1 wt% MDBS, or 0.1 wt% DMBDS was added. Data for the pristine precursor solution is also shown. (b,c,d). Comparison of the storage

(G') and loss modulus (G'') profile versus frequency for different perovskite precursor solutions: (b) pristine perovskite precursor solution; (c) precursor solution comprising 0.1 wt% MDBS, and (d) precursor solution comprising 0.1 wt% DMDBS.

Moreover, their moduli are relatively frequency-independent, reflecting the presence of a network structure that is invariant (non-relaxing) over long time scales.[30] Comparing the moduli of the perovskite solutions containing MDBS or DMDBS to the corresponding solutions comprising only the LMOGs (Figure S3), we find that both the G' and G'' moduli are higher for the MDBS-$MAPbI_3$ solutions compared to the solution comprising only MDBS. Clearly, while $MAPbI_3$ by itself is not a gelator for γBL-DMSO, it appears to synergistically strengthen the MDBS elastic network suggesting that possibly some interactions between this organic gelator and the perovskite precursor exist. In contrast, for DMDBS solutions (with and without perovskite precursor) the opposite is observed; i.e. the G' and G'' moduli are lower for the LMOG-$MAPbI_3$ solutions compared to the solution comprising DMDBS only. We attribute this to the limited solubility of DMDBS in the solvent mixture and the reduced interaction of the LMOG with the inorganic species in these solutions. The latter likely is caused by the fact that this additive features rather apolar methyl groups with which neither the solvent molecules nor the perovskite precursor can strongly interact.[31] Such a picture is supported by scanning electron microscopy (SEM) data on films prepared from precursor solutions comprising DMDBS as the LMOG (Figure S1b). We observe micron-scale crystals of DMDBS segregated from the perovskite component which can only occur when there are limited interactions between the different species. Such a morphology, not surprisingly, leads to poor devices performance (Table S1).

Solidification of the perovskite solution containing LMOGs

In order to better understand the solid-state microstructure formation especially of the MDBS systems, where a certain interplay between the additive and the precursor exists, we went on to conduct in-situ time-resolved grazing-incidence wide-angle x-ray scattering (GIWAXS)

measurements, performed during spin-coating of the perovskite formulations with and without organic gelators onto compact TiO_2.[32-35] An optimized solvent-engineering method was used, consisting of a two-step spin-coating process performed at different speeds (see experimental section for details) followed by dichloromethane (DCM) drip onto the drying layers to promote the formation of a precursor film. These can subsequently be thermally converted and crystallized into a uniform and smooth polycrystalline film.[36-38]

In-situ GIWAXS measurements were used to follow the precursor film evolution through all the phases of the multi-step method we used. In Figure S4, we show representative two-dimensional GIWAXS images taken at critical times (t = 15, 30, 45 and 90 s) after initiating the spin-coating of the different solutions, highlighting the state of the sample at different moments. We first discuss pristine solutions comprising no additives to highlight certain specific features of the development of perovskite thin films when deposited from solution.[35] Specifically, the data taken at t = 15 and 30 s show evidence of a disordered precursor phase formation (q < 6 nm^{-1}) which subsequently crystallizes (t = 45 and 90 s) as indicated by formation of diffraction rings at q= 4.7 nm^{-1}, 5.2 nm^{-1} and 6.6 nm^{-1}. Weak scattering features are also visible at q = 9.4 nm^{-1} and 10.3 nm^{-1}, corresponding, respectively, to PbI_2 and perovskite diffractions.[39,40]

We traced the time evolution of these various features using solutions of different additive content azimuthally integrating (see Figure S5) each GIWAXS snapshot taken with a time-resolution of 400 ms. We plot the 2D-intensity maps in Figures 3a, b and c, respectively, for pristine, 0.1 wt% and 0.5 wt% MDBS/perovskite precursors solutions. The x-axis represents the time scale, the y-scale represents q (radial), and the z-scale is representative of intensity. Individual q-plots taken at t = 15, 30, 45 and 90 s, respectively, are also shown in Figures 3d-gwith the insets of (e)-(g) focusing on the 8 < q < 11 nm^{-1} range. Having a close look at the data for the sample comprising no LMOG, we observe a broad scattering feature (q < 6 nm^{-1}; peak ~3.5 nm^{-1}) which dynamically evolves during the initial 40 s of spin-coating,

subsequently forming sharp scattering features (q = 4.7, 5.2 and 6.6 nm^{-1}) that can be assigned to a crystalline precursor solvate that starts to form even prior to DCM drip at ~55 s. The disordered precursor phase existing in the early stages is believed to be a sol-gel precursor phase with mesoscale order with a dominant length scale of ~2 nm; its crystallization at t > 40 s is accompanied with the formation of lead iodide and perovskite crystalline phases, for which low-intensity peaks are visible in Figure 3a and 3f. The integrated intensities and FWHM of the diffraction features are summarized in Table 1.

For samples containing MDBS, we find that the disordered sol-gel precursor scattering differs significantly, as does the onset of ordered precursor solvate formation.

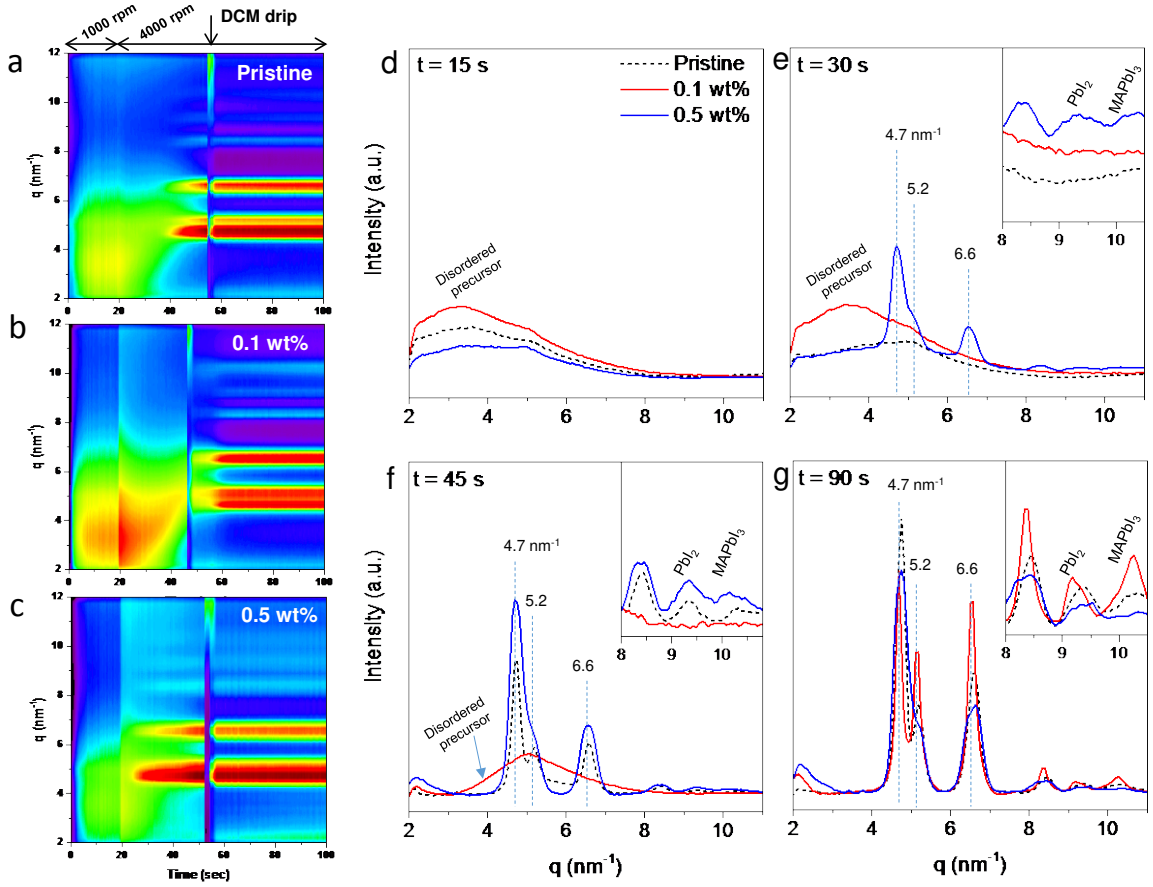

Figure 3. 2D-intensity maps during film formation from(a) the pristine prevoskite precursor solution, and (b,c) solutions comprising 0.1 wt% (b) and 0.5 wt% MDBS (c), respectively. Dripping time variations of 5 seconds and less fall within the experimental error of the measurements and was found not to affect device performance.

Individual *q*-plots taken at (d) *t* = 15 s, (e) *t* = 30 s, (f) *t* = 45 s and (g) *t* = 90 s. Insets of (e)-(g) focuson the 8 <*q*< 11 nm^{-1} range.

Table 1. Integrated intensities and FWHM of the diffraction features recorded for MDBS-based systems

Pristine					**0.1 wt%**					**0.5 wt%**				
Peak nm^{-1}	FWHM / nm^{-1} (Integrated intensity / cts)				Peak nm^{-1}	FWHM / nm^{-1} (Integrated intensity / cts)				Peak nm^{-1}	FWHM / nm^{-1} (Integrated intensity / cts)			
	30s	**45s**	**60s**	**90s**		**30s**	**45s**	**60s**	**90s**		**30s**	**45s**	**60s**	**90s**
4.7	-	0.24 (91)	0.26 (189)	0.26 (212)	4.7	-	-	0.19 (64)	0.18 (106)	4.7	0.4 (119)	0.41 (230)	0.44 (281)	0.44 (287)
5.2	-	0.32 (29)	0.45 (103)	0.42 (106)	5.2	-	-	0.22 (51)	0.21 (92)	5.2	-	-	-	-
6.6	-	0.31 (42)	0.35 (109)	0.35 (116)	6.6	--	-	0.24 (98)	0.23 (117)	6.6	0.37 (40)	0.45 (96)	0.51 (132)	0.4 (196)
9.4	-	0.39 (3.2)	0.5 (8.6)	0.75 (17.4)	9.4	-	-	0.57 (5)	0.54 (7.6)	9.4	-	0.48 (9)	0.57 (8.4)	13 (0.7)
10.3	-	0.98 (7.6)	0.53 (6.9)	0.54 (6.3)	10.3	-	-	0.38 (14.8)	0.38 (13)	10.3	1.1	1.1 (7.8)	1.1 (4.7)	0.7 (1.1)

In systems comprising 0.1 wt% MDBS, the disordered precursor scattering is more intense, indicating more metal-solvent coordination in solution. The precursor crystallization occurs ~50 s after the initial spin-coating process (~10 s later than pristine perovskite) and therefore post-DCM drip (3b), suggesting that the LMOG promotes solvent-solute interactions. However when 0.5 wt% MDBS is added (3c), the disordered sol-gel scattering feature is significantly suppressed, the crystalline solvate forms much earlier, nearly ~25 s after spin coating starts and well before DCM drip.

In this scenario, crystallization occurs only ~25 s after the spin-coating that is well before the DCM drip. [NB. For systems not comprising any LMOG crystallization on-set of crystallization is found to be around ~40 s.] Clearly the addition of 0.1 wt% MDBS promotes formation of a disordered precursor phase and enhances this phase's longevity as compared with the pristine formulations. Increasing the amount of MDBS to 0.5 wt% hinders formation of this disordered precursor phase and leads to an early onset of the precursor solvate

crystallization. Since the state of the PbI_2 and perovskite phases appears to be linked to the fate of the precursor solvate crystallization and whether it occurs post-drip (as in 0.1 wt% -MDBS formulations) or pre-drip (as in the 0.5 wt%-MDBS formulations) we further analyzed the scattering features of the various films at 90 s (Figure 5g, Table 1). The as-cast films formed using 0.1 wt% MDBS have sharper $MAPbI_3$ diffraction features than the other samples, as well as the sharpest precursor solvate diffraction features. The perovskite peak in the as-cast samples comprising 0.1 wt% MDBS shows the lowest FWHM of 0.38 nm^{-1} compared with 0.54 nm^{-1} for films cast from pristine precursor solutions and 0.7 nm^{-1} for samples with 0.5 wt% MDBS. This suggests that excessive MDBS addition disrupts the formation of a disordered sol-gel precursor in solution and hinders the crystallization of the ordered precursor solvate as compared with pristine and 0.1wt% MDBS solutions. Meanwhile, that addition of an optimum amount of MDBS leads not only to more homogeneous structures with respect to grain size but also the largest crystallites. In fact, all other diffractions features display the lowest FWHM in systems comprising 0.1wt% MDBS.

Thermal conversion and microstructure

The importance of what type of precursor solvate phase forms in as-cast films stems from the fact that this seems to determine the final microstructure and morphology of the polycrystalline perovskite film that develops during annealing/precursor conversion. We scrutinized this hypothesis further conducting annealing experiments. We find that when heating thin films produced from the various solutions investigated here to 100 °C under N_2, a striking difference in microstructure can be observed between perovskite films produced from pristine solutions and those comprising, respectively, 0.1 and 0.5wt% of MDBS (Figure 4).

Upon heating, the additives show a strong tendency to crystallize into fibrillar structures (as reported before, see Ref.31) even in presence of the perovskite precursors. These structures seem to induce the crystallization process of the perovskite phase at lower temperature compared to samples where no LMOG was added: at 60°C for perovskite/0.1 wt%-MDBS

structures and at 40°C for perovskite/0.5 wt%-MDBS films.

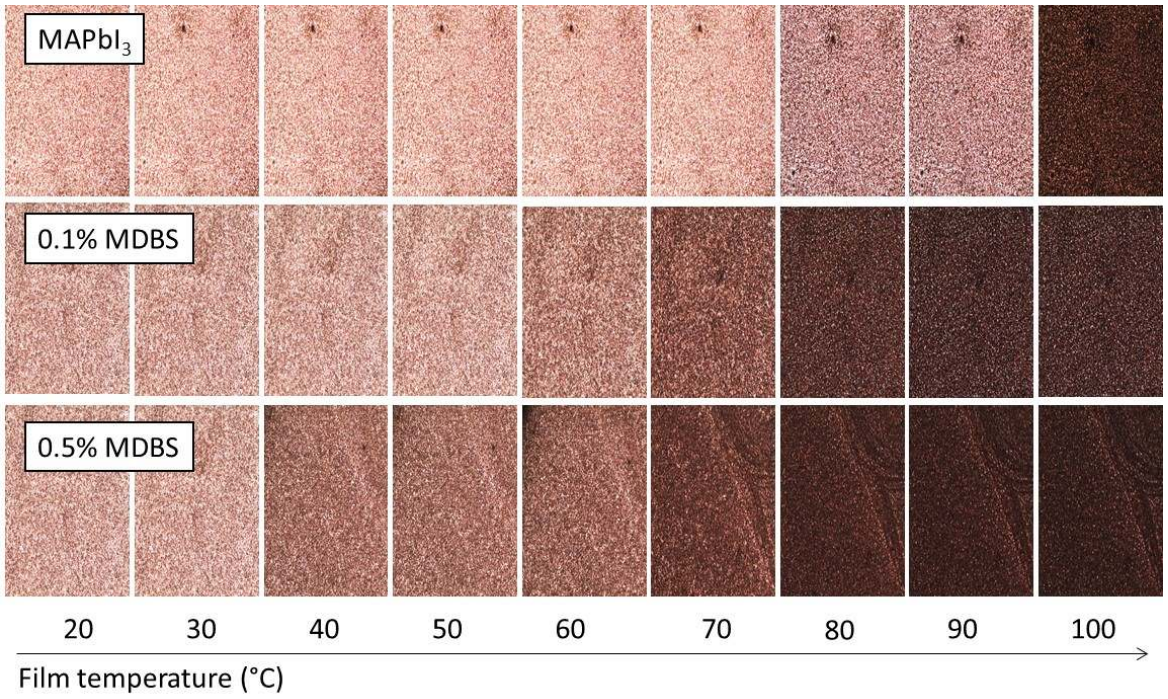

Figure 4. Optical micrographs taken at increasing temperatures of films prepared from pristine perovskite solutions and solutions comprising 0.1wt% MDBS and 0.5wt% MDBS.

These observations agree with the evolution of the storage modulus G' with temperature (see Figure S6), which relatively rapidly increases at temperatures above 60 °C for systems to which LMOGs were added, while for the pristine perovskite precursors solution a steep increase of G' (which we attribute to crystallization) occurs only at temperatures > 80 °C. This suggests that the addition of LMOG can affect the nucleation/assembly-process of the perovskite species through gel-network formation,[31] allowing the crystallization of perovskites to occur at lower temperatures.

This finding is supported by differential scanning calorimetry (DSC) measurements on the different precursors solutions. Figure 5 shows the DSC heating thermograms measured at 10°C/min, where the endotherm related to solvent evaporation has been subtracted in order to isolate the perovskite crystallization exotherm. While we find noticeable crystallization

exotherms both for the neat $MAPbI_3$ and $MAPbI_3$/0.1wt%-LMGO systems, this feature displays a somewhat earlier onset (see Table S2) and is somewhat more pronounced when MDBS was used as the additive.

Deducing the crystallization enthalpy ΔH_c from the area of the respective exotherms (based on an extrapolated horizontal baseline aligned to the asymptotic value of the DSC signal at the end of the reaction), we find that ΔH_c for $MAPbI_3$/0.1wt%-MDBS is significantly higher than for $MAPbI_3$ (respectively, −115 ± 1 kJ/mol and−82 ± 4 kJ/mol– see inset in Figure 5 and Table S2). This indicates that crystalline films of a higher degree of crystallinity are realized when using the MDBS additive in the optimum amount. It also suggests that more stable structures are produced. In fact, a higher enthalpy measured for the perovskite formation process: PbI_2 + MAI → $MAPbI_3$, has previously been attributed to be a sign for the development of a more stable perovskite structure.[41,42] The reason is that a higher enthalpy gain leads to a higher thermodynamic stability of the resulting perovskite compound.[43]

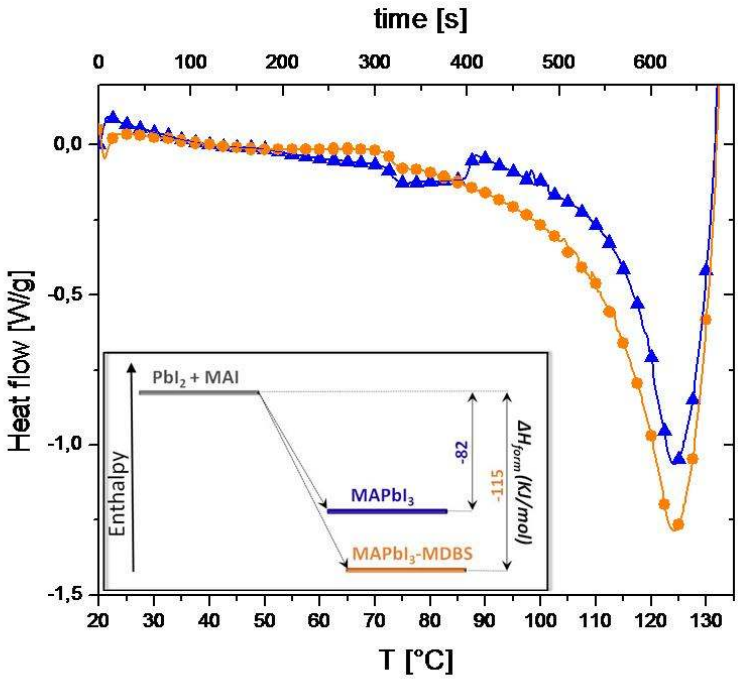

Figure 5. DSC thermograms, where the endotherms related to the solvent evaporation has been subtracted in order to isolate the perovskite crystallization exotherm of pristine $MAPbI_3$solutions and systems where 0.1 wt% of MDBS was added. Inset: Representative schematic indicating the different enthalpy of formation for $MAPbI_3$ and $MAPbI_3$-MDBS systems.

The lower standard deviation found for ΔH_c for system with MDBS (Table S2) is in addition is a sign for a more reproducible crystallization process.

Introduction of MDBS has additional benefits. The narrower grain size distribution and on average larger crystalline coherence of crystals that seems to be realizable in systems comprising this LMOG according to our X-ray data (smaller FWHM) and that likely is a direct consequence of the nucleation effect of MDBS on the perovskite precursor, leads to the formation of a more compact film (Figure 6a). This effect contributs to a two-fold increase of the $MAPbI_3$/0.1wt%-MDBS film absorption in the UV-visible wavelength regime compared to films prepared without additives of comparable thickness (160 nm; see Figure 6b). It is worth to note that the thickness of our perovskite films is relatively low compared to active layers generally used for device fabrication (350-400 nm).[44] Such thin films are as required for the realization of semitransparent solar cells, which typically are required to display an average visible transmittance (AVT) between 22% and 30%.[26, 45-48] This renders our films, featuring an AVT = 25% (Figure S7) at thickness of about 160nm, attractive for building integration purposes.

An enhanced moisture resistance compared to samples prepared without LMGOs is also observed. Exposing perovskite films produced from a pristine precursor solution as well as samples where 0.1wt% MDBS was added to 70% relative humidity (room temperature; ambient air) for 15 days, we observe a severe degradation of perovskite structure without additives. This is reflected in the significant increase in intensity of the (001) PbI_2 diffraction measured in WAXS (Figure S8), which becomes comparable to the (110) $MAPbI_3$ reflection at 14.08°. In contrast, the aged $MAPbI_3$/0.1wt%-MDBS films display a PbI_2 diffraction of rather low intensity, implying a much lower degree of decomposition. This reduced moisture sensitive of the latter samples likely is a direct consequence of (i) the more stable energy state of $MAPbI_3$ structures produced with MDBS as additive (see Figure 5b), and (ii) the formation

of a more compact film (Figure 6a) that make the polycrystalline film less accessible to hydration/decomposition reactions and to the infiltration of moisture.

Photovoltaic application

As already briefly alluded to above, the presence of MDBS –perhaps not surprisingly– strongly affects the properties and performance of perovskite-based solar cells. Our results are summarized in Table 2 and Figure 6c where we also present a schematic illustration of the planar FTO-TiO_2-perovskite/MDBS (160 nm)-spiro-MeOTAD (200 nm)/Au device architecture we utilized here.

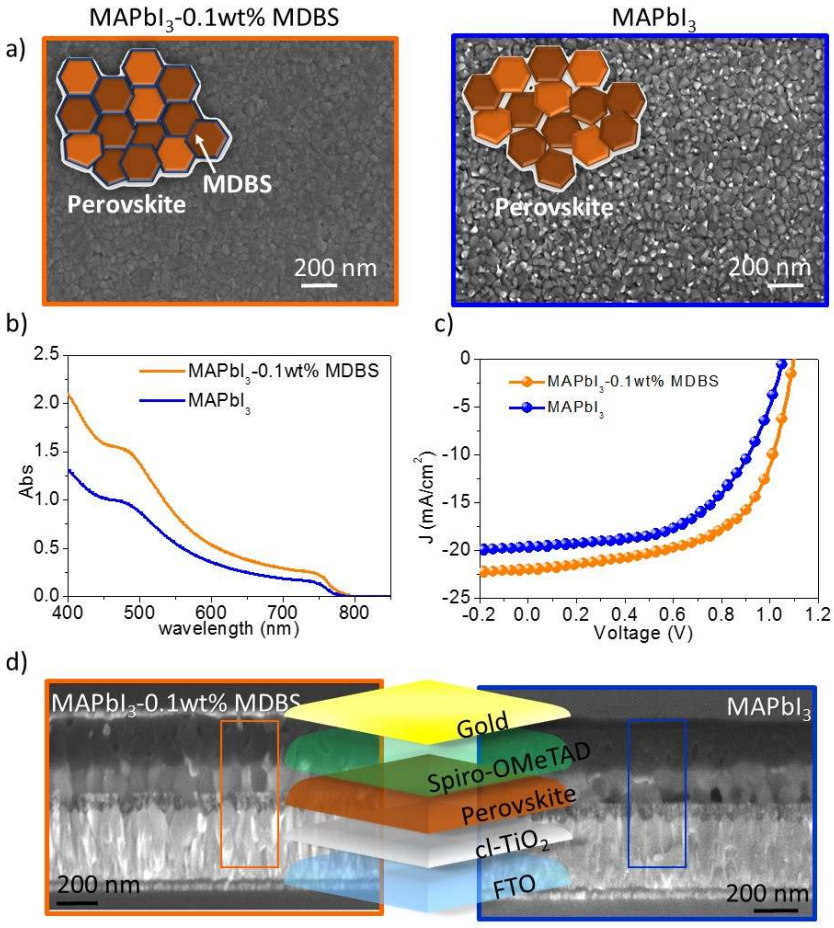

Figure 6. (a) SEM top view of films prepared with pristine perovskite precursor solutions and solutions comprising 0.1 wt% MDBS. TiO_2 substrates were used for this purpose. (b) Uv-vis absorption spectra of such films; (c) Current–voltage characteristics for champion devices prepared without (blue) and with 0.1 wt% MDBS (orange). The devices were measured under AM 1.5 at one sun. (b) SEM cross-sections of corresponding devices to which a schematic of the photovoltaic device architecture is overlaid.

Table 2. Figure of merit of devices fabricated from solutions comprising varying amounts of MDBS: open-circuit voltage (V_{OC}), short-circuit current density (J_{SC}), fill factor (FF), and PCE.

	V_{oc} (V)	J_{sc} (mA/cm^2)	FF	PCE
$MAPbI_3$	1.06	20.0	0.56	11.5
$MAPbI_3$/0.1 wt%-MDBS	1.10	22.0	0.60	14.5
$MAPbI_3$/0.5 wt%-MDBS	0.94	19.6	0.52	9.6

Immediate observations that can be made are: (i) the PCE increases from 11.5 % for devices prepared without gelator to 14.5% for cells comprising 0.1 wt% MDBS. (ii) Devices where MDBS was introduced display a significantly reduced hysteresis (Table S3). (iii) The reproducibility of device performances and their stability over time increases when MDBS was used for their fabrication. Indeed, a very small device-to-device standard deviation (0.5%) is found which is drastically lower to what we observe for cells prepared from pristine solutions (1.6%; see Figure S9), along an improved stability of PV performance within an aging period of 9 weeks (Table S4).

This superior photovoltaic performance that is observed for the devices from solutions comprising the additive, on the one hand, can be attributed to the formation of a very dense perovskite layer caused by the presences of MDBS (Figure 6a). This can have a few likely benefits: such a dense active layers can prevent undesirable recombination processes that occur through direct contact between TiO_2 and a hole transporting layer; it, thus, assists in increasing the charge collection efficiency and the fill factor, FF. On the other hand, enhancing the light-harvesting capacity of the active layer has a direct impact on the extracted current, resulting also in an average improvement in the power conversion efficiency. (Figure 6c; Table 2) It is worth noting in this context that the thicknesses of the $MAPbI_3$ layers with and without MDBS were comparable (160 ± 10 nm; Figure 6d) and in line with the thicknesses used for the fabrication of semitransparent solar cells.[26, 45-48] Thereby the efficiency of our MDBS-containing devices is higher than for solar cells of similar

thicknesses described in litterature so far. For instance, della Gaspera et al.[26] reported a maximum efficiency of 10.1% for cells with a perovskite thickness of ~140 nm embedded in a similar device architecture as used here. This thickness corresponds to an average visible transmittance (AVT) of 16%. Our devices, where the perovskite thickness is ~160 nm, feature an AVT value of 25% (Figure S7) and a maximum PCE of, respectively, 11.5% (reference device) and 14.5% ($MAPbI_3$-MDBS), rendering the use of LMOGs as processing additive highly promising for the realization of semitransparent solar cells.

We seem also to learn about the structural requirements that lead to optimum device performance. For instance, we find that pristine $MAPbI_3$ annealed for 10 minutes at 100 °C display the same PV performance of $MAPbI_3$/0.1 wt%-MDBS system annealed for half of the time (5 minutes) at the same temperature (Figure S10a). This beneficial behavior is likely due the crystallization of the perovskite layer occurring earlier in the presence of MDBS. However, best solar cells for both systems are obtained with films annealed for 10 minutes (Figure 6c). These conditions lead to perovskite/MDBS-based films that still contain a small amount of PbI_2 (Figure S10b). The presence of some PbI_2 may be beneficial because it might passivate the thin-film architecture. Previous reports have, for instance, shown that upon thermal annealing, PbI_2 species can be preferentially confined at the grain boundaries of thin-film structures leading to successful passivation of them. This assists in controlling the carrier behavior along the heterojunction. More generally, our data suggests that use of LMOGs may allow to substantially shorten currently used annealing protocols.[49]

Finally, we verified the performance of devices prepared with various content of MDBS. The best performance is observed for cells comprising 0.1 wt% MDBS – *i.e.* a very minute amount, while higher contents of MDBS leads to performance degradation even though the additive still strongly influences the nucleation and growth of the perovskite phase. Clearly, an optimum can be realized where the additive produces ideal supramolecular assemblies[31,50]

for templating perovskite crystals growth, whereas at higher MDBS content more branched and less oriented structures appear to form within the perovskite film.

3. Conclusions

We demonstrated that commercially available organic gelators can be successfully used to control the crystallization process of perovskite precursor solutions and films through the formation of a fibrillary 3D-network. This network affects the crystallization thermodynamics of the precursor species and assists in lowering its crystallization temperature. It also renders perovskite formation more stable. Moreover, the presence of an optimal (minute) amount of MDBS (0.1 wt%) promotes the sol-gel process at the early stages of perovskite ink solidification delaying the formation of the crystalline precursor solvate, but results in a more crystalline precursor phase than other conditions. In contrast, too much of the additive accelerates precursor solvate formation, which seems to be undesirable for creating compact and highly crystalline structures. Subsequent annealing converts the solvated film into structures comprised of the perovskite phase. The importance of what type of precursor solvate phase forms in as-cast films stems from the fact that this seems to have beneficial implications on the final microstructure and morphology of the polycrystalline perovskite. Intriguingly the gel-like material created through use of LMOGs enables the formation of more compact films when flat TiO_2 was used as substrate. This appears to make the perovskite drastically more robust towards exposure to moisture. The impact on the crystallization process has also important implications for device fabrication, where the use of organic gelators in future may assist in shortening the thermal annealing protocol. This could become beneficial when going to larger-scale device processing. These benefits come without compromising device performance. Indeed, we demonstrate that the use of MDBS improves the PCE of planar solar cells from 11.5% to 14.5% (at a thickness of 160 nm only), while also a dramatically reduced hysteresis is observed for the systems that comprise the additive.

Clearly, our approach allows at the same time to *i)* achieve very small device-to-device standard deviations, *ii)* improve stability to moisture of the final material compared to systems where no LMOG was added, *iii)* reduce hysteresis for planar *n-i-p* solar cells, and *iv)*lower the crystallization temperature below 100 °C. Our findings, thus, suggest that the use of LMOGs during the processing of perovskite-based materials can be a simple and effective method towards the robust and reliable fabrication of perovskite solar cells.

4. Experimental Section

Materials. All materials were purchased and used as received. Spiro-MeOTAD was purchased from Lumtec and PbI_2, Lead (II) iodide ultra-dry 99.999% (metals basis), from Alfa Aesar.CH_3NH_3I (MAI) was synthesized according to a reported procedure.[4] CH_3NH_3 (27.86 ml, 40% in methanol, TCI) and hydroiodic acid (30 ml, 57 wt% in water, Aldrich) were mixed at 0 °C and stirred for 2 h. The precipitate was recovered by evaporation at 50 °C for 1 h. The product was washed with diethyl ether three times and finally dried at 60 °C in a vacuum oven for 24 h. 1,3:2,4-di-O-methyl-benzylidene-D-sorbitol(MDBS, Millad 3940) and 1,3:2,4-bis(3,4-dimethyldibenzylidene)sorbitol (DMDBS, Millad 3988).

Optical microscopy. Perovskite solution with and without nucleating agents was prepared and stirred for 2 h at 90 °C before use. These stock solutions were coated onto bl-TiO_2/FTO substrate by a consecutive two-step spin-coating process at 1,000 and 4,000 r.p.m for 10 and 60 s, respectively with a dipping of dicloromethane at 10 sec to the end with a final film thickness of approximately 160 nm. They were annealed at various temperatures in a nitrogen environment.

Rheological analysis. The complex and steady shear viscosities of our perovskite materials were determined using an Anton Paar Phisica MCR 301 instrument equipped with measuring cone plate geometry (CP25-1 with 24.980 mm diameter and angle 1°). First, dynamic frequency spectra were conducted in the linear viscoelastic regime of the samples, as

determined from dynamic stress sweep measurements. Dynamic stress sweeps were conducted at a constant frequency of 1 Hz. The dynamic frequency sweep experiments were then carried out to obtain the complex shear viscosity (η*, Pa s), storage modulus (G'), and loss modulus (G'') over a frequency range of 0.1–600 rad/ s at 20 °C. The steady shear viscosity was also measured as a function of the shear rate in a range of 0.01–1,000 s^{-1}.

The complex dynamic viscosity is defined by:

$\eta^* = G^* / i\omega$

where G* is the complex modulus and ω is the angular frequency.

So $|\eta^*| = |G^*| / \omega$.

The complex shear modulus $G^*(\omega) = G'(\omega) + iG''(\omega)$ is defined by the relationship

$\sigma(\omega) = G^*(\omega)\gamma(\omega)$, where $\sigma(\omega)$is the stress in response to a strain $\gamma(\omega)$.

So the complex dynamic viscosity is defined in terms of the real and imaginary parts of G*(ω): $\eta^*(\omega) = G''(\omega)/\omega + iG'(\omega)/\omega$

The most frequently cited correlation between the apparent viscosity and the complex dynamic viscosity was formulated in ref. 51 as the well known empirical Cox-Merz rule:

$\eta(\gamma') = |\eta^*(\omega)|_{\omega=\gamma'}$

This useful correlation is used to convert a measurement of the steady state viscosity, η (γ'), to the modulus of the complex dynamic viscosity, η*(ω).

SEM. The SEM imaging was performed by the MERLIN Zeiss SEM FEG instrument at an accelerating voltage of 5 kV, using an In-lens detector.

DSC analysis. Dynamic DSC scans were performed on perovskite precursors solutions by a differential scanning calorimeter (DSC Mettler Toledo 622). About 6 µl of liquid samples were put into opened aluminum flat disks and heated from 20 up to 200 °C at different scan rate (0.5, 2, 5,10 °C/min) under nitrogen atmosphere flow at 60 mL/min.

XRD. The XRD spectra of the prepared films were measured with a PAN analyticalX'Pert-PRO Materials Research Diffractometer using graphite-monochromated CuK α radiation (λ = 1.5405 Å).

GIWAXS The in situ GIWAXS experiments were conducted in ambient environment (R.H. ~20%) at D1 beam line at the Cornell High Energy Synchrotron Source (CHESS) following the protocol described in ref. 35 . For spin coating, a custom-built spin coater was used with kapton tape as a protection from solution splashing. A Pilatus 200K area detector was used as the detector. The exposure time was set to 0.4 s. The solvent drip was performed remotely from outside the hutch.

Device fabrication and characterization. Glass substrates (Visiontech) and FTO-coated glass substrates (Solaronix) were cleaned by ultrasonication in a deionized water, 2-propanol and acetone. Substrates were treated to the TL1-washing procedure (washed in double distilled water (Milli-Q water), hydrogen-peroxide (H_2O_2) and ammonia (NH_3) 5:1:1 v/v (at 80°C for 10 minutes) toremove organic contamination, then rinsed ten times in water prior next depositions. A 80 nm-thick TiO_2 dense hole-blocking layer(ETL) was deposited on glass/FTO by spin coating two times at 3,000 rpm for 60 sec and annealed at 125°C using a commercial titanium diisopropoxidebis(acetylacetonate) solution(75% in 2-propanol, Sigma-Aldrich) diluted in butanol (0,15M) for 10 minutes and one time at 3,000 rpm for 60 sec and annealed at 520°C using a commercial titanium diisopropoxidebis(acetylacetonate) solution(75% in 2-propanol,Sigma-Aldrich) diluted in butanol (0,3M). The prepared MAI and commercial ultra-dry PbI_2, Alfa Aesar, were stirred (ratio 1:1) in a mixture of γ-butyrolactone (γBL) and DMSO (2:1vol/vol; γBL, ≥99%; DMSO, 99.8%; Sigma-Aldrich) at 60 °C for 12 h, to obtain a 40wt% solution. The perovskite precursor solution containing MDBS or DMDBS were prepared by adding 0.1wt%, 0.5wt% or 1wt% of either DBS derivative (with respect to MAI+PbI_2 weight) to 40wt% perovskite precursors solution, followed by heating these mixtures to 125 °C while stirring until clear solutions were obtained. Solutions were then

allowed to cool to room temperature. Both pristine perovskite precursor solution and the once containing DBS derivatives were coated onto either glass or TiO_2/FTO substrate by a consecutive two-step spin-coating process at 1,000 and 4,000 r.p.m for 20 and 60 s, respectively with a dripping of dichloromethane at 10 sec to the end. After spin-coating, the films were annealed on a hotplate at 100 °C for 10 min. After cooling to room temperature, a spiro-MeOTAD solution was spin-coated on the perovskite layer at 2,500 r.p.m. for 45 s. Spiro-MeOTAD solution was prepared by dissolving 90 mg of spiro-MeOTAD in 1 ml chlorobenzene (99.8%, Sigma Aldrich), to which were added 28.8 µl of 4-tert-butylpyridine (96%, Sigma-Aldrich), 17.5 µl lithium bis (trifluoromethanesulfonyl)imide (LiTFSI) solution (520 mg LI-TSFI in 1 ml acetonitrile, 99.8%, Sigma-Aldrich). This fabrication process was carried out under controlled conditions in a glove-box atmosphere and a temperature between 20 and 25 °C. Finally, 80 nm gold was thermally evaporated on top of the device at a pressure of 5×10^{-6} mbar to form the back contact. The active area of the complete device was 0.09 cm^{-2}.The devices were characterized after 3h exposure to ambient conditions using a Keithley 2400 Source Measure Unit and AirMass 1.5 Global (AM 1.5G) solar simulator (Newport 91160A) with an irradiation intensity of 100 mW/cm^2. The solar simulator irradiance was set to 100 mW/cm^2using a thermopile radiant power meter with fused-silica window (Spectra Physics Oriel, model 70260). All devices are tested using 100 ms delay time.

Supporting Information

Supporting Information is available from the Wiley Online Library or from the author.

Acknowledgements

S.C. and A.L. acknowledge Regione Puglia and ARTI for funding FIR – future in research projects “PeroFlex” project no. LSBC6N4 and “HyLight” project no. GOWMB21. The authors acknowledge the project Progetto di ricerca PON MAAT (Project Number: PON02_00563_3316357) and PERSEO-“PERovskite-based Solar cells: towards high Efficiency and lOng-term stability” (Bando PRIN 2015-Italian Ministry of University and

Scientific Research (MIUR) Decreto Direttoriale 4 novembre 2015 n. 2488, project number 20155LECAJ) for funding. A.R. and S.M. gratefully acknowledge SIR project "Two-Dimensional Colloidal Metal Dichalcogenides based Energy-Conversion Photovoltaics" (2D ECO), Bando SIR (Scientific Independence of young Researchers) 2014 MIUR Decreto Direttoriale 23 gennaio 2014 no. 197 (project number RBSI14FYVD, CUP: B82I15000950008) for funding. The authors acknowledge Sonia Carallo for technical support. N. D. T. acknowledges support from the National Science Foundation's International Research Fellowship Program (OISE-1201915) and the European Research Council's Marie Curie International Incoming Fellowship under grant agreement number 300091. N.S. is by a European Research Council Starting Independent Researcher Fellowship under grant agreement number 279587.

Received: ((will be filled in by the editorial staff))
Revised: ((will be filled in by the editorial staff))
Published online: ((will be filled in by the editorial staff))

References

[1] J. Burschka, N. Pellet, S.-J Moon, R. Humphry-Baker, P. Gao, M. K.,Nazeeruddin, M. Gratzel, *Nature* **2013**, *499* (7458), 316-319.

[2] S. Ryu, J. H. Noh, N. J. Jeon, Y. Chan Kim, W. S.Yang, J. Seo, S. I. Seok, *Energy & Environmental Science* **2014**,*7* (8), 2614-2618.

[3] W. S. Yang, J. H. Noh, N. J. Jeon, Y. C. Kim, S. Ryu, J. Seo,S. I. Seok, *Science* **2015**, *438*, 1234-1237.

[4] M. M. Lee,J. Teuscher, T. Miyasaka, T. N. Murakami, H. J. Snaith, *Science* **2012**, *338* (6107), 643-647.

[5] H. Zhou, Q. Chen, G. Li, S. Luo, T.-b. Song, H.-S. Duan, Z. Hong, J. You, Y. Liu, Y. Yang, *Science* **2014**, *345* (6196), 542-546.

[6] V. L. P. Guerra, D. Altamura, V. Trifiletti, S. Colella, A. Listorti, R. Giannuzzi, G. Pellegrino, G. G. Condorelli, C. Giannini, G. Gigli, A. Rizzo, *J. Mat. Chem. A* **2015**, 3, 20811-20818.

[7] S. Colella, E. Mosconi, G. Pellegrino, A. Alberti, V. L. P. Guerra, S. Masi, A. Listorti, A. Rizzo, G. G. Condorelli, F. De Angelis, G. Gigli, *J. Phys. Chem. Lett.*, **2014**, 5 (20), 3532-3538.

[8] A. Genco, F. Mariano, S. Carallo, V. L. P. Guerra, S. Gambino, D. Simeone, A. Listorti, S. Colella, G. Gigli, M. Mazzeo, *Advanced Electronic Materials*, **2016**, DOI:10.1002/aelm.201500325.

[9] S. Colella, M. Mazzeo, A. Rizzo, G. Gigli, A. Listorti, *The Journal of Physical Chemistry Letters*, **2016**, 7 (21), 4322-4334.

[10] M. Xiao,F. Huang, W. Huang, Y. Dkhissi, Y. Zhu, J. Etheridge, A. Gray-Weale, U. Bach, Y.-B. Cheng, L., A Spiccia, *Angewandte Chemie International Edition* **2014**, *53* (37), 9898-9903.

[11] N. J. Jeon, J. H. Noh,W. S. Yang, Y. C. Kim, S. Ryu, J. Seo, S. I. Seok, *Nature* **2015**, *517* (7535), 476-480.

[12] H. D. Kim, H. Ohkita, H. Benten, S. Ito, *Advanced Materials* **2015**, DOI:10.1002/adma.201504144.

[13] B. Conings, L. Baeten, C. De Dobbelaere, J. D'Haen, J. Manca, H.-G.Boyen, *Advanced Materials* **2014**, *26* (13), 2041-2046.

[14] A. Dualeh, N. Tétreault, T. Moehl, P. Gao, M. K. Nazeeruddin, M. Grätzel, *Advanced Functional Materials* **2014**, *24* (21), 3250-3258.

[15] S. Masi, S. Colella, A.Listorti, V. Roiati, A. Liscio, V. Palermo, A. Rizzo, G. Gigli, *Scientific Reports* **2015**, *5*, 7725.

[16] P.-W. Liang, C.-Y., Liao, C.-C. Chueh, F. Zuo, S. T. Williams, X.-K.Xin, J.Lin, A. K. Y.Jen, *Advanced Materials* **2014**, *26* (22), 3748-3754.

[17] C. Zuo, L. Ding, *Nanoscale* **2014**, *6* (17), 9935-9938.

[18] S. Masi, A. Rizzo, F. Aiello, F. Balzano, G. Uccello-Barretta, A. Listorti, G. Gigli, S. Colella, *Nanoscale*, **2015**, 7, 18956-18963.

[19] Q. Wang, Y. Shao, Q. Dong, Z. Xiao, Y. Yuan, J. Huang, *Energy & Environmental Science* **2014**, *7* (7), 2359-2365.

[20] H.-B. Kim, H. Choi, J. Jeong, S. Kim, B. Walker, S. Song, J. Y. Kim, *Nanoscale* **2014**, *6* (12), 6679-6683.

[21] W. Nie, H. Tsai, R. Asadpour, J.-C. Blancon, A. J. Neukirch, G. Gupta, J. J. Crochet, M. Chhowalla, S. Tretiak, M. A. Alam, H.-L. Wang, A. D. Mohite, *Science* **2015**, *347* (6221), 522-525.

[22] X. Li, M. Ibrahim Dar, C. Yi, J. Luo, M. Tschumi, S. M. Zakeeruddin, M. K. Nazeeruddin, H. Han, M. Grätzel, *Nat Chem* **2015**, *7* (9), 703-711.

[23] N. Mohmeyer, P. Wang, H.-W. Schmidt, S. M. Zakeeruddin, M. Gratzel, *Journal of Materials Chemistry* **2004**, *14* (12), 1905-1909.

[24] N. D. Treat, J. A. Nekuda Malik, O. Reid, L. Yu, C. G.Shuttle, G.Rumbles, C. J. Hawker, M. L.Chabinyc, P. Smith, N. Stingelin, *Nat Mater* **2013**, *12* (7), 628-633.

[25] P. Terech, R. G. Weiss, *Chemical Reviews* **1997**, *97* (8), 3133-3160

[26] E. Della Gaspera, Y. Peng, Q. Hou, L. Spiccia, U. Bach, J. J. Jasieniak, Y.-B. Cheng, *Nano Energy* **2015**, *13*, 249-257.

[27] J. Li, K. Fan, L. Niu, Y. Li, J. Song, *The Journal of Physical Chemistry B* **2013**, *117* (19), 5989-5995.

[28] Y. Zhao, K. Zhu, *The Journal of Physical Chemistry C* **2014**, *118* (18), 9412-9418.

[29] G. E. Eperon, V. M. Burlakov, P. Docampo, A. Goriely, H. J. Snaith, *Advanced Functional Materials* **2014**, *24* (1), 151-157.

[30] A. Y. Malkin, *Journal of Non-Newtonian Fluid Mechanics* **2013**, *192*, 48-65.

[31] B. O. Okesola, V. M. P. Vieira, D. J. Cornwell, N. K. Whitelaw, D. K., Smith, *Soft Matter* **2015**, *11* (24), 4768-4787.

[32] K. W. Chou, B. Yan, R. Li, E. Q. Li, K. Zhao, D. H. Anjum, S. Alvarez, R. Gassaway, A. Biocca, S. T. Thoroddsen, A. Hexemer, A. Amassian, *Advanced Materials* **2013**, *25* (13), 1923-1929.

[33] K. Wei Chou, H. Ullah Khan, M. R. Niazi,. B. Yan, R. Li, M. M. Payne, J. E. Anthony, D.-M. Smilgies, A. Amassian, *Journal of Materials Chemistry C* **2014**, *2* (28), 5681-5689.

[34] M. Abdelsamie, N. D. Treat, K. Zhao, C. McDowell, M. A. Burgers, R. Li, D.-M. Smilgies, N. Stingelin, G. C. Bazan, A. Amassian, *Advanced Materials* **2015**, *27* (45), 7285-7292.

[35] R. Munir, A. D. Sheikh, M. Abdelsamie, H. Hu, L. Yu, K. Zhao, T. Kim, O. E. Tall, R. Li, D.-M. Smilgies, A. Amassian, *Advanced Materials* **2016**, DOI: 10.1002/adma.201604113.

[36] V. Trifiletti, N. Manfredi, A. Listorti, D. Altamura, C. Giannini, S. Colella, G. Gigli, A. Rizzo, *Adv. Mat. Interface*, **2016**, DOI:10.1002/admi.201600493.

[37] A. Giuri, S. Masi, S. Colella, A. Kovtun, S. Dell'Elce, E. Treossi, A. Liscio, C. Esposito Corcione, A. Rizzo, A. Listorti, *Adv. Funct. Mat*, **2016**, DOI:10.1002/adfm.201603023.

[38] T. Miletić, E. Pavoni, V. Trifiletti, A. Rizzo, A. Listorti, S. Colella, N. Armaroli, D. Bonifazi, *ACS Applied Materials & Interfaces*, **2016**, 8, 27966-27973.

[39] Y.-C. Huang, C.-S. Tsao, Y.-J. Cho, K.-C. Chen, K.-M. Chiang, S.-Y. Hsiao, C.-W. Chen, C.-J. Su, U. S. Jeng, H.-W. Lin, *Scientific Reports* **2015**, *5*, 13657.

[40] K. W. Tan, D. T. Moore, M. Saliba, H. Sai, L. A. Estroff, T. Hanrath, H. J.Snaith, U. Wiesner, *ACS Nano* **2014**, *8* (5), 4730-4739.

[41] A. Buin, P. Pietsch, J. Xu, O. Voznyy, A. H.Ip, R. Comin, E. H. Sargent, *Nano Letters* **2014**, *14* (11), 6281-6286.

[42] J. Haruyama, K. Sodeyama, L. Han, Y. Tateyama, *The Journal of Physical Chemistry Letters* **2014**, *5* (16), 2903-2909.

[43] A. Buin, R. Comin, J. Xu, A. H. Ip, E. H. Sargent, *Chemistry of Materials* **2015**, *27* (12), 4405-4412.

[44] H. Zhou, Q. Chen, G. Li, S. Luo, T.-b. Song, H.-S. Duan, Z. Hong, J. You, Y. Liu, Y. Yang, *Science* **2014**, *345* (6196), 542-546.

[45] C. Roldan-Carmona, O. Malinkiewicz, R. Betancur, G. Longo, C. Momblona, F. Jaramillo, L. Camacho, H. J. Bolink, *Energy & Environmental Science* **2014**, *7* (9), 2968-2973.

[46] L. K. Ono, S. Wang, Y. Kato, S. R. Raga, Y. Qi, *Energy & Environmental Science* **2014**, *7* (12), 3989-3993.

[47] F. Fu, T. Feurer, T. Jäger, E. Avancini, B. Bissig, S. Yoon, S. Buecheler, A. N. Tiwari, *Nature Communications* **2015**, *6*, 8932.

[48] F. Guo, H. Azimi, Y. Hou, T. Przybilla, M. Hu, C. Bronnbauer, S. Langner, E. Spiecker, K. Forberich, C. J. Brabec, *Nanoscale* **2015**, *7* (5), 1642-1649.

[49] Y. H. Lee, J. Luo, R. Humphry-Baker, P. Gao, M. Grätzel, M. K. Nazeeruddin, *Advanced Functional Materials* **2015**, *25* (25), 3925-3933.

[50] J. Lipp, M. Shuster, G. Feldman, Y. Cohen, *Macromolecules* **2008**, *41* (1), 136-140.

[51] W. P. Cox, E. H. Merz, *Journal of Polymer Science* **1958**, *28* (118), 619-622.

The table of content

Organic gelators, widely used in the processing of commodity 'plastics', are applied here tohybrid halide perovskites solidification. They are shown to beneficially influence the nucleation and growth of the perovskite sol-gel precursor phase, leading to a material characterized by a higher stability to moisture and a reduced hysteresis in planar n-i-p heterojunction solar cells.

Organic gelators as growth control agents for stable and reproducible hybrid perovskite-based solar cells

Keywords: halide perovskites, organic gelators, photovoltaics

Sofia Masi,Aurora Rizzo, Rahim Munir, Andrea Listorti, Antonella Giuri,Carola Esposito Corcione,Neil D. Treat, Giuseppe Gigli,Aram Amassian, Natalie Stingelin,and Silvia Colella

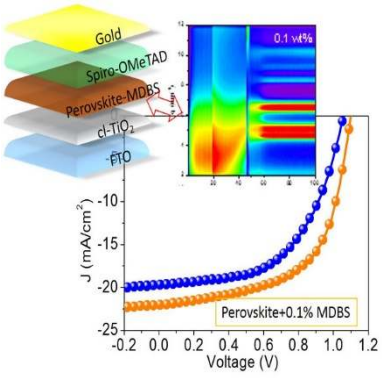

Supporting Information

Organic gelators as growth control agents for stable and reproducible hybrid perovskite-based solar cells

Sofia Masi,Aurora Rizzo, Rahim Munir, Andrea Listorti, Antonella Giuri, Carola Esposito Corcione, Neil D. Treat, Giuseppe Gigli,Aram Amassian, Natalie Stingelin,* and Silvia Colella**

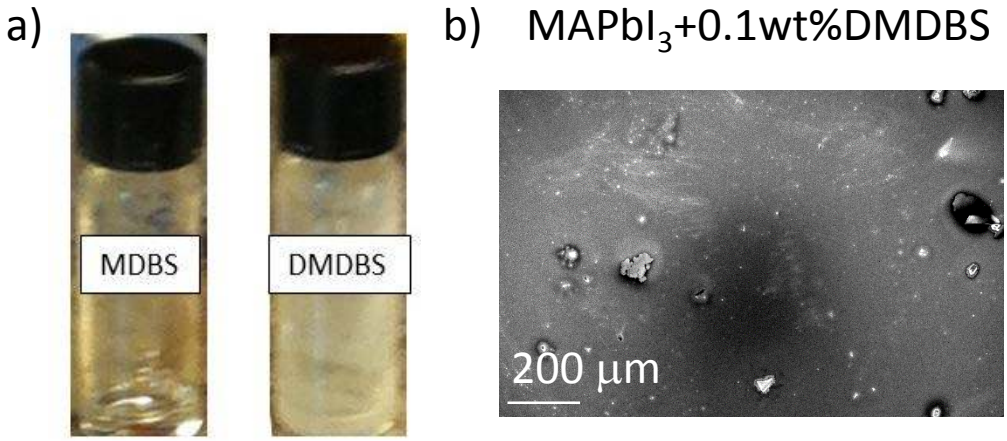

Figure S1. (a) Pictures of MDBS and DMDBS 0.5 wt% solution in γ-BL:DMSO 2:1; (b) SEM top view of $MAPbI_3$+ 0.1wt% DMDBS film on TiO_2 substrate.

Table S1. Solar cell figures of merit of devices fabricated with varying amounts of DMDBS incorporated into casting solution

	PCE (%)	FF	V_{OC} (V)	J_{SC}(mA/cm^2)	Mean ± s.d.
$MAPbI_3$-DMDBS 0.1wt%	0.7	0.28	0.61	4.0	0.7 ± 0.2
$MAPbI_3$-DMDBS 0.5wt%	0.3	0.17	0.68	2.6	0.3 ± 0.1

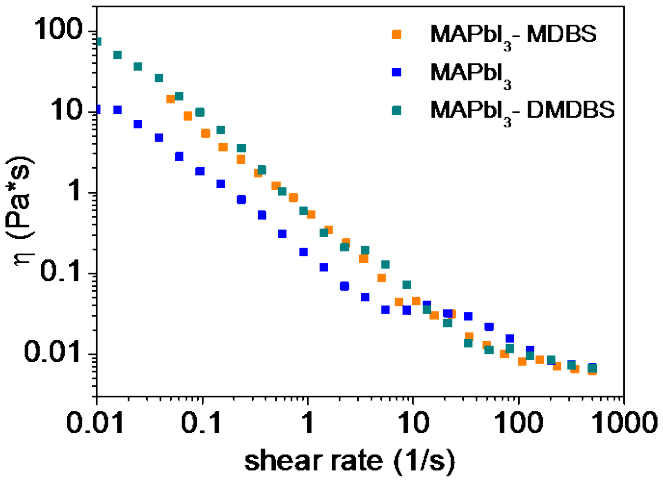

Figure S2. Shear viscosity as a function of the shear rate for $MAPbI_3$, $MAPbI_3$ + 0.1wt% MDBS and $MAPbI_3$ + 0.1wt% DMDBS.

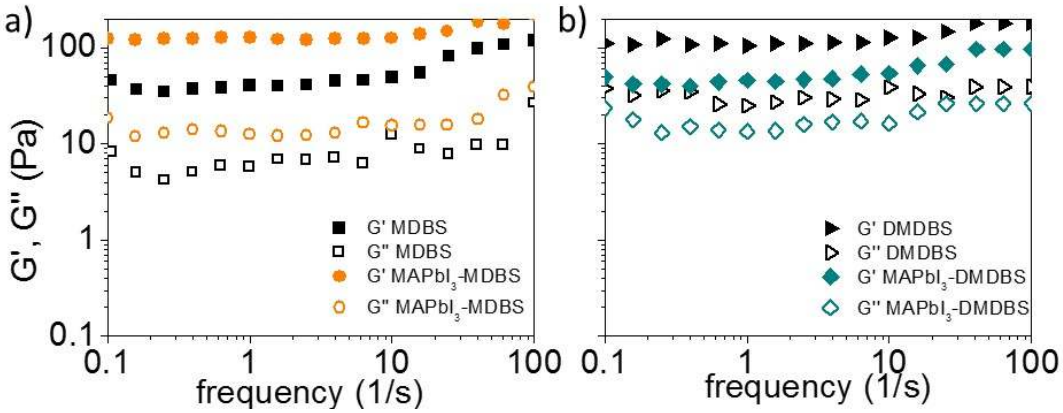

Figure S3. Comparison of the storage (G') and loss molulus (G'') profile versus frequency for a) MDBS 0.1wt% and $MAPbI_3$+ 0.1wt%MDBSand b) for DMDBS 0.1 wt% and $MAPbI_3$+ 0.1wt% DMDBS solutions.

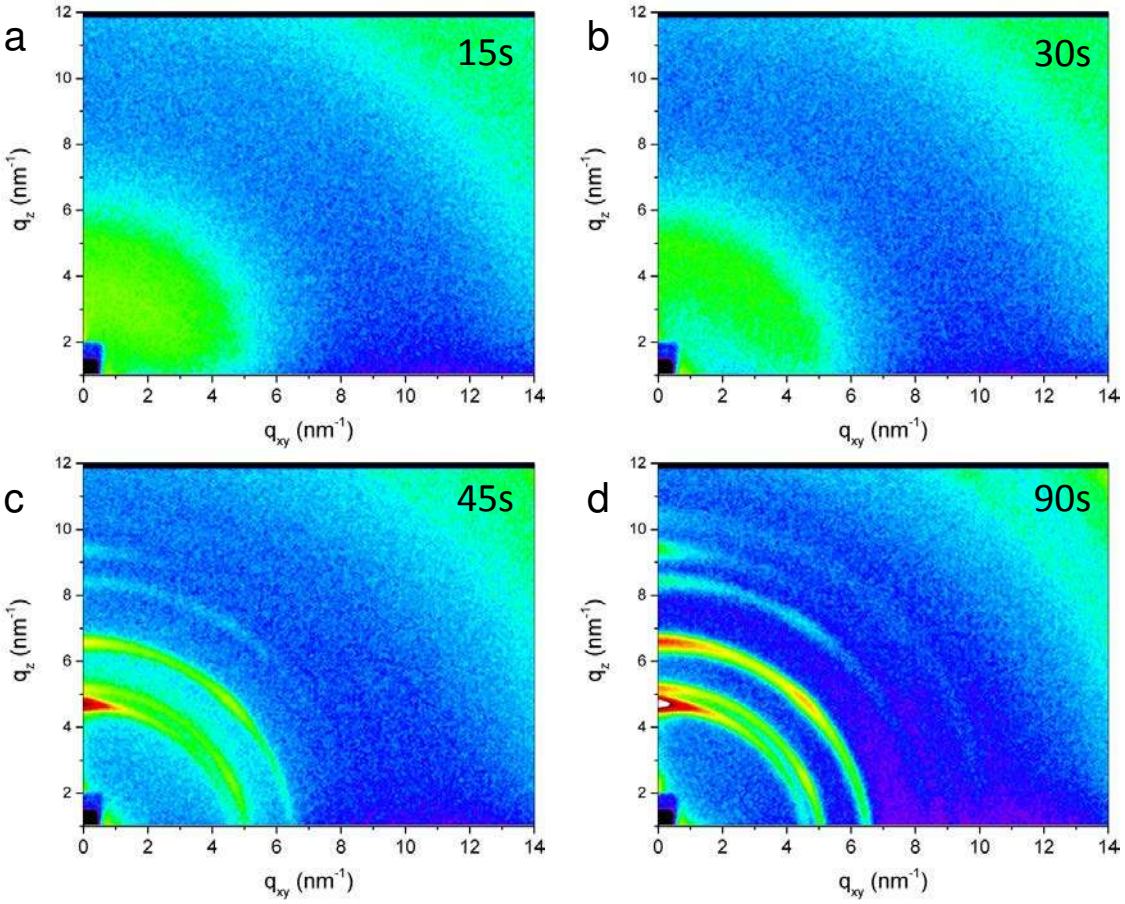

Figure S4. Two-dimensional GIWAXS images taken at key moments (t = 15, 30, 45 and 90 s) after initiating the spin-coating of the pristine solution.

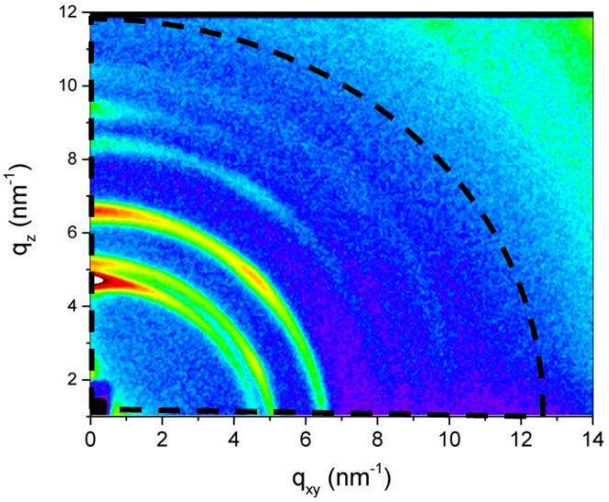

Figure S5. Two-dimensional GIWAXS image of pristine sample showing the cake integration performed on each GIWAXS image.

Table S2. Differential scanning calorimetry (DSC) parameters: starting (T onset) peak (Tpeak) and ending (T endset) temperatures at scan rate of 10°C/min for $MAPbI_3$, $MAPbI_3$/0.1 wt% MDBS and $MAPbI_3$/0.1 wt% DMDBS. The formation enthalpy (ΔH) has the same value for each scan rate.

Sample	T_{onset} (°C)	T_{peak} (°C)	T_{endset} (°C)	t_{endset}-t_{onset} (s)	Delta H (KJ/mol)
$MAPbI_3$	111	124	131	123	82±4
$MAPbI_3$+MDBS 0.1wt%	103	124	132	161	115±1
$MAPbI_3$+DMDBS 0.1wt%	112	124	131	116	72±13

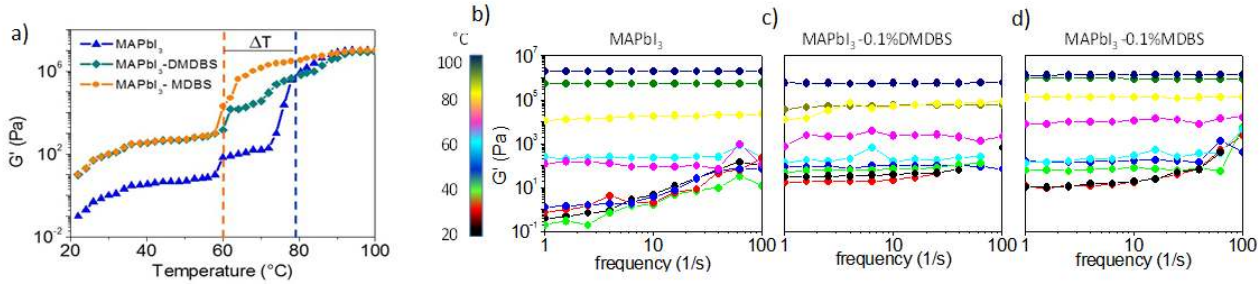

Figure S6. (a) Comparison of the storage modulus (G') at different temperature of bare perovskite solution, perovskite + 0.1 wt% MDBS solution and perovskite + 0.1 wt% DMDBS solution, at 1 Hz. G' values are taken at 1Hz from the elastic storage (G') versus frequency scans, at different temperatures, of (b) bare perovskite solution, (c) perovskite + 0.1 wt % MDBS solution and (d) perovskite + 0.1 wt % DMDBS solution.

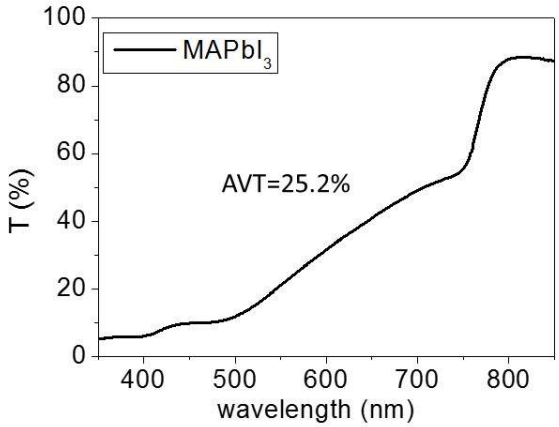

Figure S7. Average visible transmittance of perovskite film.

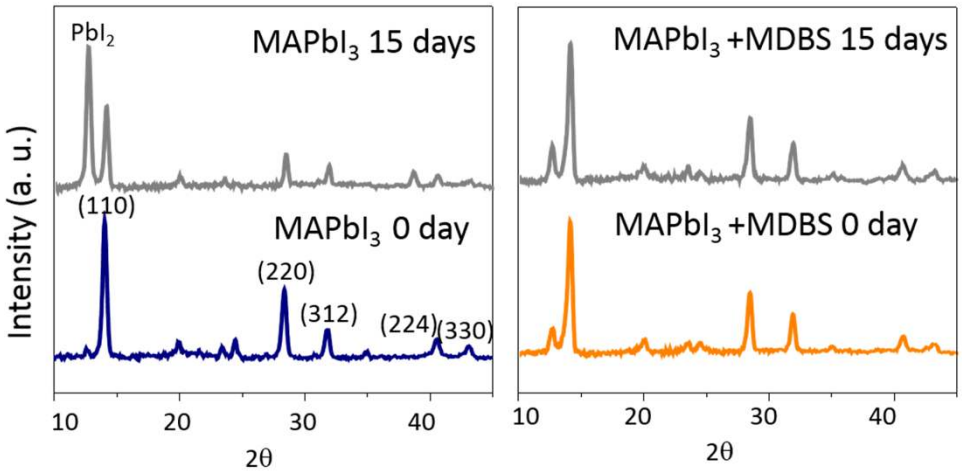

Figure S8. XRD patterns of films produced from a neat precursor solution (left) compared to structures that were produced with 0.1wt% MDBS. A comparison is shown of as prepared and aged films kept 15 day in ambient conditions, at 70 %humidity.

Table S3. Main photovoltaic parameters of cells using perovskite and perovskite-MDBS, measured by forward and reverse scans to calculate the hysteresis index.[1]

	PCE (%)	FF	Voc (V)	Jsc (mA/cm^2)	Hysteresis index
With MDBS Reverse	15.0	0.64	1.08	21.8	0.03
With MDBS Forward	14.5	0.60	1.1	22.0	
w/o MDBS Reverse	8.5	0.45	1.1	17.6	0.09
w/o MDBS Forward	11.5	0.56	1.06	20	

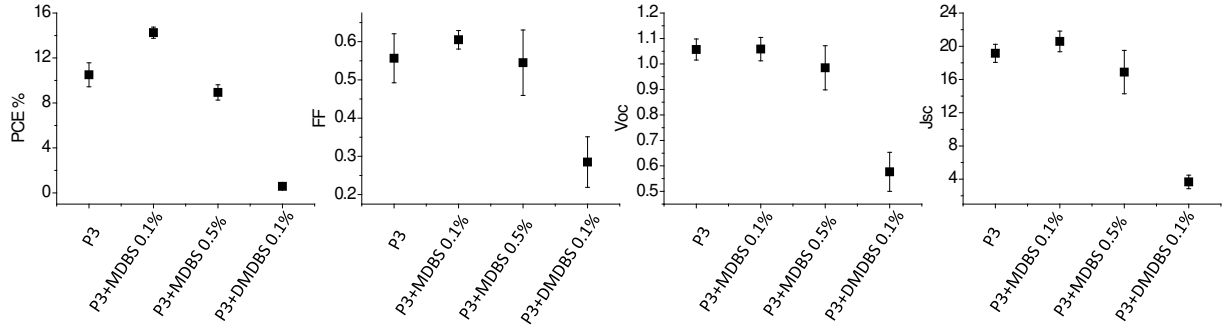

Figure S9. Statistics of PCE (%), FF, Voc and Jsc of devices based on perovskite and perovskite with different amount of MDBS layers.

Table S4. Photovoltaic parameters of perovskite based devices, with and without MDBS, over a period of two months.

$MAPbI_3$-MDBS	PCE (%)	FF	Voc (V)	Jsc (mA/cm^2)
0 week	14.5	0.60	1.10	22
4 weeks	13.4	0.67	0.98	21
9 weeks	12.6	0.60	0.93	22

$MAPbI_3$	PCE (%)	FF	Voc (V)	Jsc (mA/cm^2)
0 week	11.5	0.56	1.06	20
4 weeks	8.7	0.68	0.96	13.3
9 weeks	5.6	0.57	0.88	11.2

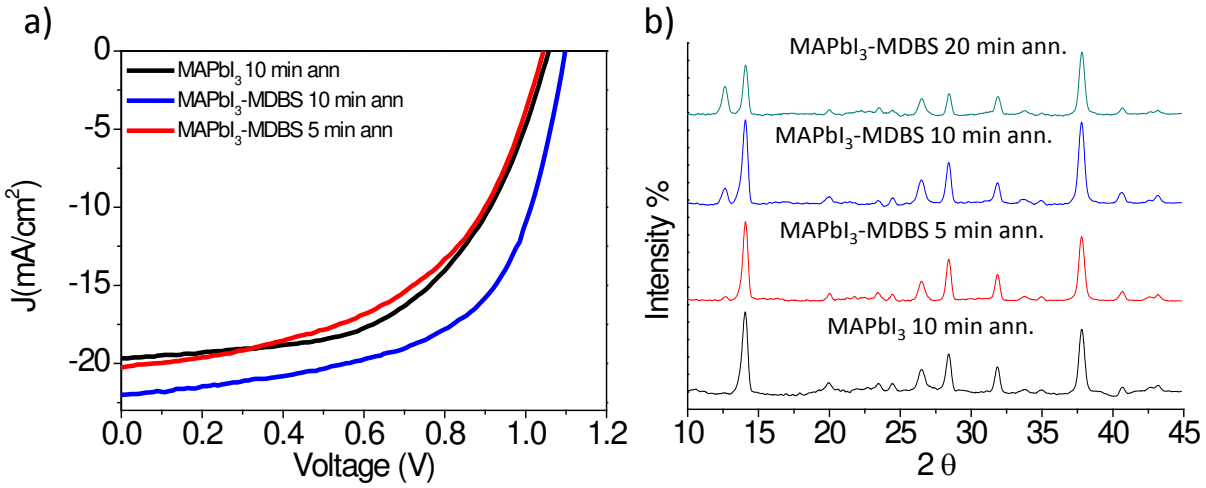

Figure S10. (a) J-V curves of device based on bare perovskite and device based on perovskite-MDBS 0.1 wt% at different annealing time; (b) corresponding XRD patterns.

[1] R. S. Sanchez, V. Gonzalez-Pedro, J.-W. Lee, N.-G. Park, Y. S. Kang, I. Mora-Sero, J. Bisquert, *The Journal of Physical Chemistry Letters* **2014**, *5* (13), 2357-2363.